



# Metals incorporated into OMS-2 lattice create flexible catalysts with highly efficient activity in VOCs combustion

Hua Deng<sup>a,b,\*</sup>, Yuqin Lu<sup>a,b</sup>, Tingting Pan<sup>a,b</sup>, Lian Wang<sup>c</sup>, Changbin Zhang<sup>c,\*\*</sup>, Hong He<sup>a,b,c</sup>

<sup>a</sup> Center for Excellence in Regional Atmospheric Environment, Key Laboratory of Urban Pollutant Conversion, Institute of Urban Environment, Chinese Academy of Sciences, Xiamen 361021, China

<sup>b</sup> University of Chinese Academy of Sciences, Beijing 100049, China

<sup>c</sup> State Key Joint Laboratory of Environment Simulation and Pollution Control, Research Center for Eco-Environmental Sciences, Chinese Academy of Sciences, Beijing 100085, China

## ARTICLE INFO

### Keywords:

Volatile organic compounds  
Catalytic oxidation  
Manganese oxide  
Octahedral molecular sieve  
Mechanism

## ABSTRACT

Catalytic combustion of different types of VOCs with various functional groups generally requires certain catalysts with high efficiency. Here, a novel manganese oxide catalyst was tuned via incorporation of small amounts of different metals, including Ce, Ir, Ag, Pd, Cu and Fe respectively, exhibiting flexible activity in the abatement of different VOC species. Pd and Ag doping was beneficial for toluene oxidation, while the addition of Cu significantly enhanced the acetone elimination performance, and Ir incorporation boosted the removal of dichloromethane. XRD, Raman, and TEM results revealed that the different metal ions were well-dispersed into the lattice of OMS-2. Elemental mapping images and ICP-OES combined with DFT calculations demonstrated that Ce, Ir, Pd, Cu and Fe were incorporated into OMS-2 by substituting for Mn on octahedral sites, and Ag could be stabilized in the tunnel of OMS-2 via replacing K ions. EXAFS results suggested that the local tunnel structures of OMS-2 were almost intact after incorporation of the different metals. Pd-OMS-2 and Ag-OMS-2 exhibited excellent activity in catalytic oxidation of toluene due to the improved reducibility and mobility of oxygen. Cu ions improved the scission of C—C bonds in acetone and Ir ions facilitated the cleavage of the C—Cl bond in dichloromethane, all of which contributed to their highly specific activity in removal of the corresponding VOCs. This work provides information on the production of highly efficient metal sites for catalytic oxidation of specific VOC species, and may assist with the design of flexible catalysts for control of miscellaneous VOCs.

## 1. Introduction

Volatile organic compounds (VOCs) are organic chemicals with low boiling points (< 250 °C) at atmospheric pressure [1,2]. It is estimated that emissions of anthropogenic VOCs in China were in the range of 26.6–28.5 Tg yr<sup>-1</sup> in 2017 [3,4]. The persistent growth and vast quantities of VOC emissions pose severe threats to both humans and the environment [1,3]. Anthropogenic VOCs are emitted from a large number of sources [4,5], including transportation, industry, solvent use and power systems. The diversity of sources leads to the complexity and difficulty of the abatement of miscellaneous VOCs via end-of-pipe control in practice [6,7].

Solvent use is one of the main contributors to the fast increase in VOC

emissions during rapid urbanization and industrialization [4]. Toluene [8], acetone [9] and dichloromethane [10] are widely encountered as hazardous VOCs from solvent use. Controlling these VOC emissions originating from solvent use is vital to protecting the air quality in China and developed countries.

Among different post-treatment technologies, catalytic oxidation has been regarded as one of the most promising candidates for the elimination of VOCs owing to its high efficiency, low levels of undesirable by-products and low cost [11,12]. It is well known that supported noble metal catalysts demonstrate excellent activity and stability in the oxidation of aromatics and aliphatic hydrocarbons [1,13]. Transition metal oxide [1,5] or confined-structure [14] catalysts are suitable for the removal of chlorinated VOCs and volatile organic sulfur compounds due

\* Corresponding author at: Center for Excellence in Regional Atmospheric Environment, Key Laboratory of Urban Pollutant Conversion, Institute of Urban Environment, Chinese Academy of Sciences, Xiamen 361021, China.

\*\* Corresponding author.

E-mail addresses: [huadeng@iue.ac.cn](mailto:huadeng@iue.ac.cn) (H. Deng), [cbzhang@rcees.ac.cn](mailto:cbzhang@rcees.ac.cn) (C. Zhang).

<https://doi.org/10.1016/j.apcatb.2022.121955>

Received 1 August 2021; Received in revised form 29 September 2021; Accepted 11 October 2021

Available online 12 September 2022

0926-3373/© 2022 Elsevier B.V. All rights reserved.

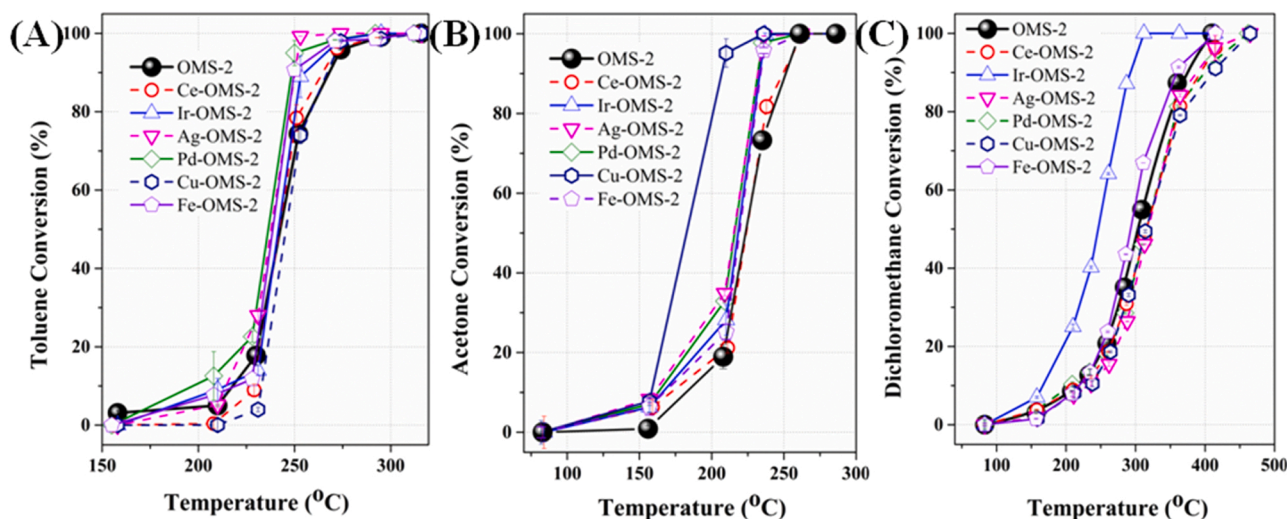


Fig. 1. Toluene (A), Acetone (B) and Dichloromethane (C) conversion over different M-OMS-2 catalysts as a function of temperature.

to their good resistance to poisoning. OMS-2 is a promising catalyst for the catalytic oxidation of VOCs due to its tunable catalytic properties and abundant resources [1,11]. Substitution with transition metals (including Ni, Zr, Ti, V, Nb etc.) [15] is the most common way to increase catalytic performance via enhancing redox activity [16]. Preparing an efficient catalyst for various VOCs is the key to VOC degradation. Apart from the emphasis on active oxygen species, the activation of specific VOC species is barely addressed in combustion.

In this study, monovalent (Ag), divalent (Cu), trivalent (Fe), and multivalent metals (including Ce, Ir, Pd) were introduced into OMS-2 to produce flexibly doped manganese oxide catalysts (M-OMS-2). Substitution with different metals gave rise to highly specific efficiency in the removal of toluene, acetone and dichloromethane correspondingly. The effects of metal incorporation on pristine OMS-2 catalysts were assessed via various techniques including XRD, BET, TEM, XANES, XPS, H<sub>2</sub>-TPR, CO-TPD, EXAFS, VOC-TPD, etc. Apart from the general important role of surface oxygen species in combustion, the enhancement of activity via the activation of the above VOC species was addressed with the help of different metal dopants. This work can benefit the design and preparation of novel catalysts with high efficiency for the abatement of specific VOC pollutants.

## 2. Materials and methods

### 2.1. Material preparation

Different metal-embedded catalysts (M-OMS-2) were prepared via a redox reaction between a Mn<sup>2+</sup> precursor and MnO<sub>4</sub><sup>-</sup> precursor [17,18]. In a typical run, different metal precursors in appropriate amounts (including Ce(NO<sub>3</sub>)<sub>3</sub>·6H<sub>2</sub>O, (NH<sub>4</sub>)<sub>2</sub>IrCl<sub>6</sub>, AgNO<sub>3</sub>, Pd(NO<sub>3</sub>)<sub>2</sub>·2H<sub>2</sub>O, Cu(NO<sub>3</sub>)<sub>2</sub>·3H<sub>2</sub>O, Fe(NO<sub>3</sub>)<sub>3</sub>·9H<sub>2</sub>O, Table S1) mixed with 18.38 g of MnAc<sub>2</sub>·4H<sub>2</sub>O were dissolved in deionized water under stirring. 12.5 mL glacial acetic acid was then added to form an acidic environment. A solution of 10.27 g KMnO<sub>4</sub> was added slowly to the above mixture under stirring (the total Mn/metal mole ratio was 40). Next, the mixed solution was maintained at 100 °C for 24 h in a 500 mL Teflon-lined autoclave. After natural cooling, a black slurry was obtained and washed with deionized water to neutral pH. Finally, the sample was annealed in a furnace at 550 °C for 3 h and then cooled to ambient temperature naturally. The final samples were denoted as Metal-OMS-2. For example, a sample denoted as Ce-OMS-2 means Ce incorporated in OMS-2. The pristine OMS-2 was also prepared by the same procedure without other metal precursor dopants for use as a control.

### 2.2. Catalytic evaluation

The catalytic oxidation of different VOC species was conducted in a continuous flow quartz reactor (8 mm i.d.) at temperatures from 150 to 450 °C. The intrinsic physical properties of different VOC species are listed in Table S2. A gaseous mixture of toluene (1000 ppm), acetone (1000 ppm) or dichloromethane (200 ppm) in air balance at a mass flow of 150 mL min<sup>-1</sup> was fed into the above reactor. Experiments on VOC mixtures (1000 ppm C<sub>7</sub>H<sub>8</sub> and 200 ppm CH<sub>2</sub>Cl<sub>2</sub> or 1000 ppm C<sub>3</sub>H<sub>6</sub>O and 200 ppm CH<sub>2</sub>Cl<sub>2</sub>) with air balance were also performed to evaluate the catalytic activity at the same flow rate. About 0.1 g of the catalysts was used for each experiment. The GHSV value was about 45,000 h<sup>-1</sup> (SV = 90,000 mL h<sup>-1</sup> g<sup>-1</sup>). The concentrations of different VOC species were analyzed online by a gas chromatograph (GC; Agilent 7890B, HP-5 capillary column) with a flame ionization detector. CO<sub>2</sub> and O<sub>2</sub> concentrations were analyzed by the same GC equipped with a thermal conductivity detector (Porapak Q and HayeSep Q column). In all the experiments, VOC conversion was calculated using the following equation:

$$\text{VOC Conversion}(\%) = \left(1 - \frac{[\text{VOC}]_{\text{out}}}{[\text{VOC}]_{\text{in}}}\right) \times 100\%$$

In order to compare the metrics and performance of various catalysts under different conditions, the reaction rates  $R_{\text{mass}}$  (mol g<sub>cat</sub><sup>-1</sup> s<sup>-1</sup>) were calculated according to the following equation [1]:

$$R_{\text{mass}} = \frac{C_{\text{VOC}} \times X_{\text{VOC}} \times V_{\text{gas}}}{m_{\text{cat}}} \quad \left(\text{mol g}_{\text{cat}}^{-1} \text{ s}^{-1}\right)$$

where  $C_{\text{VOC}}$  is the initial concentration of VOC species in the gas mixture.  $X_{\text{VOC}}$  denotes the steady-state VOC conversion.  $V_{\text{gas}}$  is the total flow rate (mol s<sup>-1</sup>), and  $m_{\text{cat}}$  is the catalyst weight (g). The molar volume of gas is 24.5 L mol<sup>-1</sup>.

### 2.3. Materials characterization

The properties of all M-OMS-2 catalysts were comprehensively studied. For instance, the crystal structure, local structure and porosity of materials were investigated by XRD, Raman and N<sub>2</sub> adsorption-desorption measurements respectively. The morphologies were revealed by TEM/HRTEM. The chemical state was probed by XPS and XAS (XANES and EXAFS). The Mn-K edges of the OMS-2 framework oxides were measured in transmission mode on the BL14W1 beam line, Shanghai Synchrotron Radiation Facility (SSRF). The surface properties were studied by H<sub>2</sub>-TPR, CO-TPD, TP-GC-MS and VOC-TPD.

**Table 1**

Comparison of toluene, acetone and dichloromethane oxidation catalysts known to exhibit good performance.

Catalysts	Concentration (ppm)	GHSV (mL/(g h))	T <sub>90</sub> (°C)	Reaction rate (μmol g <sub>cat</sub> <sup>-1</sup> s <sup>-1</sup> )	Refs.
<b>Toluene (at 190 °C)</b>					
0.2 wt% Pd/Al <sub>2</sub> O <sub>3</sub> -R	1000	60,000	208	0.14	[21]
0.27 Pt/3DOM CeO <sub>2</sub> -Al <sub>2</sub> O <sub>3</sub>	1000	20,000	198	0.12	[22]
SmMn <sub>2</sub> O <sub>5</sub>	250	60,000	228	0.017	[23]
Mn <sub>2</sub> Co <sub>1</sub> oxides	1000	60,000	236	0.034	[24]
δ-MnO <sub>2</sub>	1000	60,000	245	0.075	[25]
Cu <sub>0.7</sub> Mn <sub>2</sub> Ce <sub>0.3</sub> Ox/HTS-1	2000	10,000	275	0.041	[26]
Pd-OMS-2	1000	90,000	247	0.087	This study
Ag-OMS-2	1000	90,000	253	0.041	This study
OMS-2	1000	90,000	268	0.031	This study
<b>Acetone (at 160 °C)</b>					
CeO <sub>2</sub> /Co <sub>3</sub> O <sub>4</sub>	600	45,000	200	0.045	[27]
GdMn <sub>2</sub> O <sub>5</sub>	500	24,000	160	0.12	[28]
10 V-TiC	500	7200	292	0.082	[29]
Mn <sub>3</sub> AlO oxide	500	54,000	190	0.092	[30]
4.14 wt% Pt/TiO <sub>2</sub>	1000	40,000	195	0.11	[31]
1.61 wt% CeO <sub>2</sub> -0.05 wt% Pt/TiO <sub>2</sub>	1000	40,000	270	0.045	[31]
0.8Pt-G/@Zr	1000	60,000	210	0.082	[32]
Cu-OMS-2	1000	90,000	207	0.12	This study
Pd-OMS-2	1000	90,000	231	0.092	This study
OMS-2	1000	90,000	251	0.01	This study
<b>Dichloromethane (at 260 °C)</b>					
Co <sub>3</sub> O <sub>4</sub> /ZSM-5	1000	30,000	370	0.061	[33]
Ti-Fe oxide	1000	30,000	300	0.17	[34]
0.01 Pt-20Co/HZSM-5	600	15,000	249	0.061	[35]
Cr-Co/ZSM-5	1000	30,000	328	0.11	[36]
Phosphate-CeO <sub>2</sub>	500	15,000	300	0.056	[37]
Ir-OMS-2	200	90,000	293	0.13	This study
Fe-OMS-2	200	90,000	358	0.051	This study
OMS-2	200	90,000	375	0.041	This study

The detailed material characterization methods are described in the [Supporting information \(SI\) Text S1](#).

## 2.4. DFT calculation

Periodic DFT calculations were performed using a plane-wave method (the Vienna Ab-initio Simulation Package). The exchange-correlation functional was treated within the GGA approximation parameterized by PBE. The electron-ion interaction was described by the projector augmented wave (PAW) approach. Tight convergence of the plane-wave expansion was obtained with a kinetics energy cut-off of 400 eV. The electron configurations 2s<sup>2</sup>2p<sup>4</sup>, 3d<sup>5</sup>4s<sup>2</sup>, 3p<sup>6</sup>4s<sup>1</sup> were considered as the valence electrons for O, Mn and K respectively. Spin polarization was considered in all calculations. The convergence criteria for electronic and ionic relaxation were 10<sup>-5</sup> eV and 0.02 eV Å<sup>-1</sup>, respectively. The optimized pristine crystal lattice parameters of OMS-2 (KMn<sub>8</sub>O<sub>16</sub>) were as follows: a = b = 9.71 Å, c = 2.85 Å, and α = β = γ = 90, which are close to values given in many other reports [19,20]. Since the precursor Mn/metal mole ratio was 40 during preparation, a (1 × 1 × 5) supercell was applied to simulate the effects of ion exchange. Brillouin zone sampling used the Monkhorst-Pack scheme with a 3 × 3 × 2 mesh of k-points. Different metal ions can substitute for the Mn or K ions in OMS-2. The total energy was calculated as follows:

$$E_{total} = E_{M-OMS-2} + E_{K/Mn}$$

Lower  $E_{total}$  values indicate that the corresponding K or Mn substitution is more favorable energetically.

## 3. Results and discussion

### 3.1. Catalytic activity of M-OMS-2 catalysts

The conversion of toluene, acetone and dichloromethane over M-OMS-2 catalysts as a function of temperature is illustrated in [Fig. 1](#). Incorporation of different metals induced obvious differences in activity. Noble metal addition including Pd, Ag and Ir gave rise to good activity for toluene combustion. For instance, the conversion rate for Pd-OMS-2 was 95 % at a reaction temperature of 254 °C, which was 21 % higher than that of pristine OMS-2, as shown in [Fig. 1\(A\)](#). All metal dopants in this study were effective for acetone oxidation, because all light-off curves of M-OMS-2 moved toward the lower temperature zone, as exhibited in [Fig. 1\(B\)](#). Among them, Cu-OMS-2 demonstrated the highest activity in the elimination of acetone. The T<sub>90</sub> of Cu-OMS-2 was decreased by about 50 °C compared to pristine OMS-2. Incorporation of Ir significantly improved the performance for dichloromethane removal. The T<sub>90</sub> of Ir-OMS-2 was decreased by about 80 °C compared to pristine OMS-2, as shown in [Fig. 1\(C\)](#). Pristine OMS-2 exhibited clear advantages in terms of the tunability of its catalytic properties [11,16].

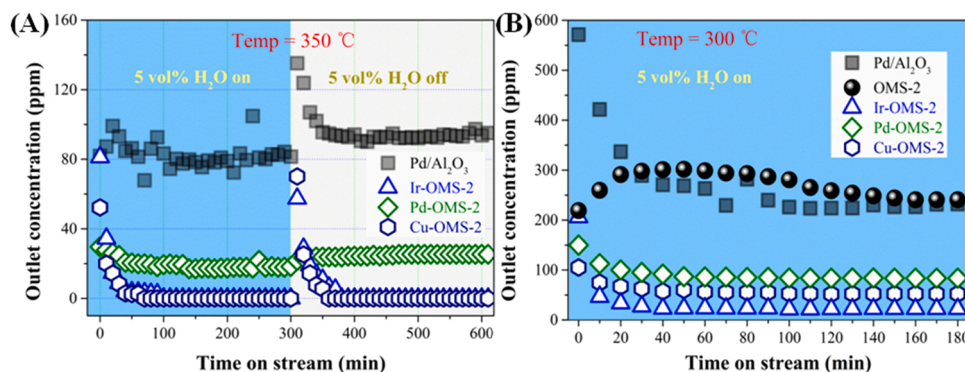


**Fig. 2.** Stability test of different M-OMS-2 and 1 wt% Pd/Al<sub>2</sub>O<sub>3</sub> catalysts at 350 °C (A), 300 °C (B); conditions: 1000 ppm toluene, 1000 ppm acetone, 150 ppm dichloromethane and, 5 vol% H<sub>2</sub>O (when used, SV = 90,000 mL h<sup>-1</sup> g<sup>-1</sup>).



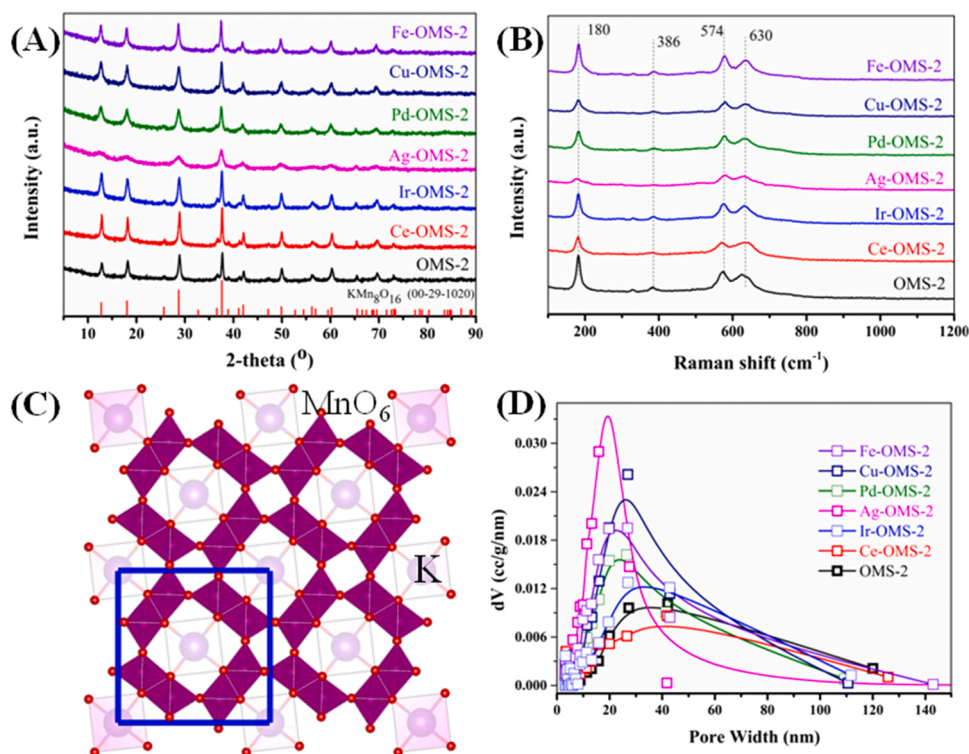


Fig. 3. XRD patterns (A), Raman spectra (B), model of OMS-2 (C), and pore-size distribution (D) for the series of M-OMS-2 catalysts.

The reaction rates of selected M-OMS-2 and catalysts that have been reported to have good performance for different types of VOCs are listed in Table 1. The  $T_{50}$  and  $T_{90}$  for individual VOCs and mixtures are listed in Table S3. The light-off curves for binary mixtures are exhibited in Figs. S1 and S2. Pd, Cu and Ir addition led to the highest specific activity in the oxidation of toluene, acetone and dichloromethane respectively. The temperatures for complete combustion of toluene, acetone and dichloromethane were about 220, 270 and 350 °C respectively in binary mixtures. Since C—Cl bond breaking requires high energy or high reaction temperature, dichloromethane is the decisive component in the combustion of mixtures. Therefore 350 °C and 300 °C were applied in the stability test respectively in Fig. 2. The outlet concentration in Fig. 2 is the sum of all VOCs in this study. Owing to the recalcitrance of Cl-VOCs, the mixture outlet gas is dominated by dichloromethane species.

The tolerance of selected M-OMS-2 and classical Pd/Al<sub>2</sub>O<sub>3</sub> catalysts (Fig. S3) to water vapor was evaluated by stability testing as illustrated in Fig. 2. Ir-OMS-2 and Cu-OMS-2 exhibited excellent stability and activity compared to Pd/Al<sub>2</sub>O<sub>3</sub> in combustion of VOC mixtures, and 5 vol % H<sub>2</sub>O addition barely influenced the performance at a reaction temperature of 350 °C. On decreasing the reaction temperature to 300 °C, the VOC mixture removal efficiency varied as follows: Ir-OMS-2 > Cu-OMS-2 > Pd-OMS-2 > OMS-2 ≈ Pd/Al<sub>2</sub>O<sub>3</sub>. It is well known that water vapor can act as a surface cleaner to depress chlorine deposition via the

Deacon reaction [34,35]. In this way, catalyst deactivation could be hindered. Therefore, good stability can be obtained with the addition of water vapor.

A long-term high-temperature stability test was performed over the selected Ir-OMS-2 catalyst. The results are exhibited in Fig. S4. The VOC mixtures were completely converted. The CO<sub>2</sub> yield was almost equal to the theoretical value. Moreover, the effluents were absorbed by a 0.0125 M NaOH solution. The chlorine products were analyzed by an ion chromatograph (DIONEX, ICS-3000, AS11-HC). Only Cl<sup>-</sup> was observed, without ClO<sub>2</sub>, indicating that the desirable product HCl is dominant among the chloride products. After a long-term stability test, the used Ir-OMS-2 catalyst was investigated by XRD, XPS and TEM, with the results exhibited in Figs. S5 and S6. The active Ir-OMS-2 catalyst also exhibited excellent stability. Used Ir-OMS-2 not only maintained the diffraction pattern of OMS-2 as illustrated in Fig. S5 (A), but also showed the same distinct lattice fringes at about 0.70 nm as shown in Fig. S6 (B). Moreover, mapping images indicated that all elements in used Ir-OMS-2 are homogeneously dispersed. The chemical states of Mn and Ir were unchanged after the long-term test, which confirms the good stability of the Ir-OMS-2 catalyst.

Table 2

Textural parameters of all catalysts derived from N<sub>2</sub> physisorption results and contents of K, Mn and metals determined by ICP-OES.

Sample	BET	Pore volume	Pore diameter	K (wt%)	Mn (wt%)	Radius (pm)	Metal (wt%)
	(m <sup>2</sup> /g)	(mL/g)	(nm)	ICP	ICP	Mn <sup>4+</sup> 67 Mn <sup>3+</sup> 72	ICP
OMS-2	59.5	0.63	42.1	5.6	56.9	K <sup>+</sup> 152	—
Ce-OMS-2	52.9	0.46	41.9	4.9	55.1	Ce <sup>4+</sup> 101	4.3
Ir-OMS-2	72.7	0.61	27.1	5.1	53.8	Ir <sup>4+</sup> 76.5	4.4
Ag-OMS-2	123.7	0.56	20.2	3.9	55.2	Ag <sup>+</sup> 129	4.4
Pd-OMS-2	93.9	0.58	26.6	5.2	53.4	Pd <sup>4+</sup> 75.5	4.6
Cu-OMS-2	98.0	0.71	26.9	5.0	55.8	Cu <sup>2+</sup> 87	4.1
Fe-OMS-2	96.9	0.60	26.8	5.2	53.6	Fe <sup>3+</sup> 78.5	4.5



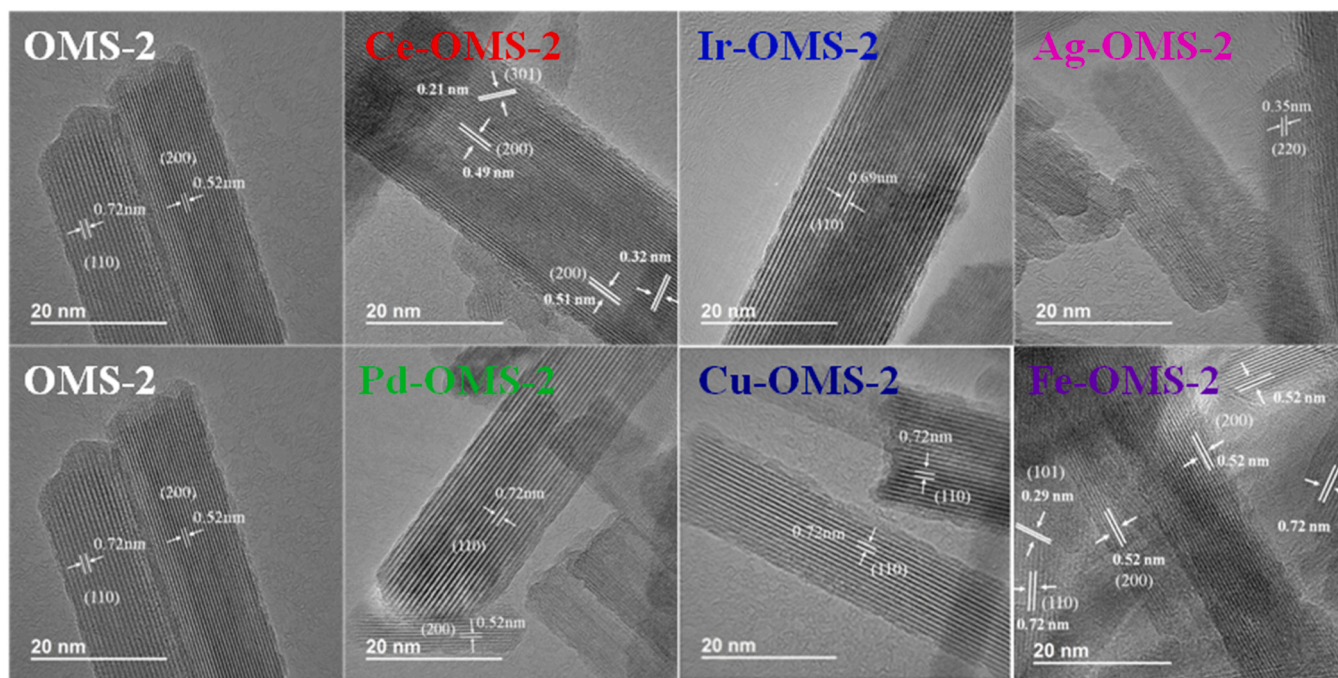


Fig. 4. HRTEM images of different M-OMS-2 catalysts.

### 3.2. Structural properties of M-OMS-2 modified by different metals

Different metals incorporated into the lattice of OMS-2 may give rise to significant structural variations. XRD and Raman data were combined to learn the nature of these structural changes. As illustrated in Fig. 3(A) and (B), all M-OMS-2 samples maintained the diffraction pattern of OMS-2 (ICDD no. 00-29-1020) [18,20], and the four distinct Raman peaks characteristic of OMS-2 at 180, 386, 574 and 630  $\text{cm}^{-1}$  were all preserved [17,38]. The XRD and Raman results are consistent with each other, revealing that the main OMS-2 crystal structure was intact after different metals were embedded. It is worthy of note that the diffraction and Raman peaks of Ag-OMS-2 were broadened and decreased in intensity compared to the other M-OMS-2 samples. This is consistent with other studies [39] owing to a nanoscale size-reduction phenomenon. Fig. 3(C) demonstrates the structure model of OMS-2, illustrating that the replacement of  $\text{K}^+$  by  $\text{Ag}^+$ , with smaller radius, may result in the shrinkage of the OMS-2 crystal lattice [17]. OMS-2 materials generally have characteristic stacked mesopore structures [17,39,40]. Metal addition clearly enhanced the mesopore structure and specific surface area, as illustrated in Fig. 3(D) and Table 2. For instance, the BET surface areas of Pd-OMS-2, Ag-OMS-2 and Cu-OMS-2 increased by factors of 1.5, 2.1 and 1.6, respectively. The increases in surface area and adsorption sites are favorable for the catalytic degradation of VOCs.

The morphologies of M-OMS-2 samples were investigated by TEM as shown in Fig. S7. A rod-like fibrous morphology, typical of OMS-2 materials [20,38,40], was retained even after the addition of different metals. The HRTEM images shown in Fig. 4 reveal that all M-OMS-2 samples exhibited well-defined lattice fringes. The widths of neighboring lattice fringes are about 0.72 and 0.49 nm, corresponding to the (110) and (200) surfaces of OMS-2 [15,41], which are frequently observed for different M-OMS-2 catalysts. No other metal particles can be observed. The HRTEM results were consistent with the above XRD and Raman spectra, confirming that the crystalline structure of OMS-2 is preserved after the addition of different metals. In order to learn the fate of the different metals in the lattice of OMS-2, the mapping images of Mn, O, K, and doped metals were obtained and are demonstrated in Fig. 5 and Fig. S8. Pd, Ir, Cu, Ce, Ag, Fe and skeleton Mn and K ions are homogeneously dispersed in the corresponding OMS-2 lattice structures.

This indicates that all doped metals are uniformly embedded into the lattice of OMS-2.

The bulk contents of different metal ions in M-OMS-2 are presented in Table 2. The K amounts in Ag-OMS-2 are remarkably lower than the ideal content of OMS-2 (5.4 wt%) [17,41], confirming that K ions in these materials in hexahedral coordination are replaced by Ag ions. As listed in Table 2, the ionic radii of Ir, Pd, Cu and Fe species are close to the radius of  $\text{Mn}^{4+}$ , all of which are considerably smaller than that of  $\text{K}^+$ . This suggested that Ir, Pd, Cu and Fe species embedded in OMS-2 lattice via substituting on Mn octahedral sites. The radius of Ce ions is between those of  $\text{Mn}^{4+}$  and  $\text{K}^+$ . It can be deduced that Ce species can partially occupy both K and Mn sites in OMS-2 [18]. To explore this further, DFT simulation was applied to elucidate the ion substitution effect. Generally, two types of ions sites in OMS-2 can be adopted by guest metal species. The optimized models of M-OMS-2 formed via replacing K hexahedral sites and Mn octahedral sites in OMS-2 are plotted in Fig. S9 and Fig. S10. Comparison of the total energy is illustrated in Fig. 6. This agreed well with the above experiment showing that Fe, Ir, Pd, Cu and Ce are energetically favored to substitute for Mn ions to form newly created heteroatom octahedra. Ag species show no energy preference for occupying K or Mn sites in OMS-2. Therefore, the theoretical and experimental results are consistent with each other, revealing that Ag species are stabilized at K hexahedral sites and other metal ions occupy octahedral sites of OMS-2 (Fig. S11 and Table S4).

### 3.3. The chemical states and surface properties of M-OMS-2

The above results indicate that Ce, Ir, Ag, Pd, Cu and Fe are all embedded into the lattice of OMS-2. The chemical states of the different metals were examined by XPS, as shown in Fig. 7. The red peaks are characteristic of  $\text{Ce}^{4+}$ , and the blue peaks can be attributed to  $\text{Ce}^{3+}$  [18, 31] as shown in Fig. 6(A). The ratio of  $\text{Ce}^{4+}$  to  $\text{Ce}_{\text{total}}$  is about 60 %, suggesting that most Ce ions are in the highest oxidation state. Deconvolution of the Ir  $4f_{7/2}$  and satellite peaks shows sets of peaks at 61.7 and 62.9 eV respectively, and the major peak accounted for up to 70 % as depicted in Fig. 7(B). This is consistent with another report [42] that Ir ions exist in the form of  $\text{Ir}^{4+}$ . The Ag  $3d_{5/2}$  XPS binding energy for Ag-OMS-2 is 367.6 eV, as shown in Fig. 7(C), which could be attributed

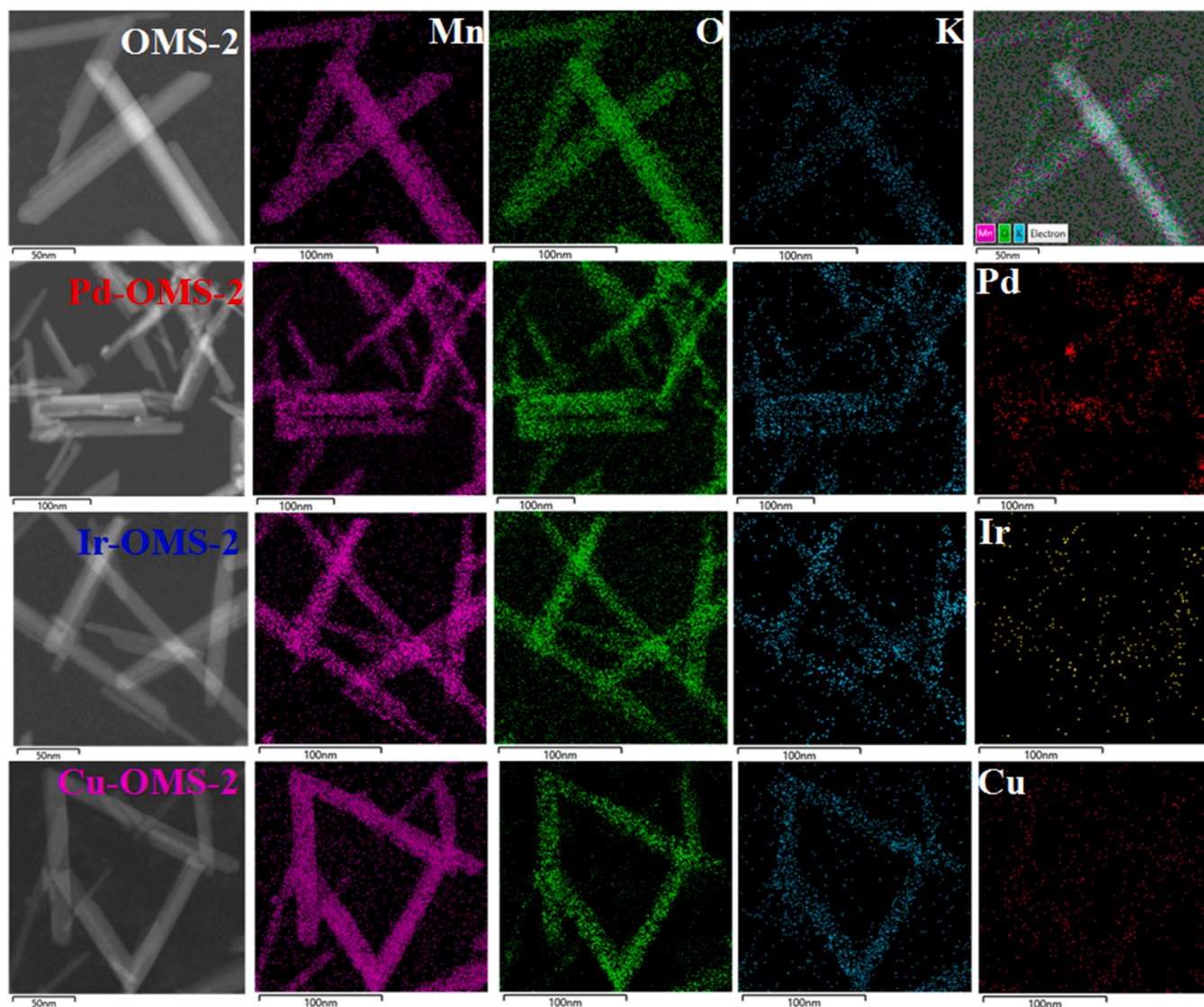


Fig. 5. Mapping images of OMS-2, Pd-OMS-2, Ir-OMS-2 and Cu-OMS-2 catalysts.

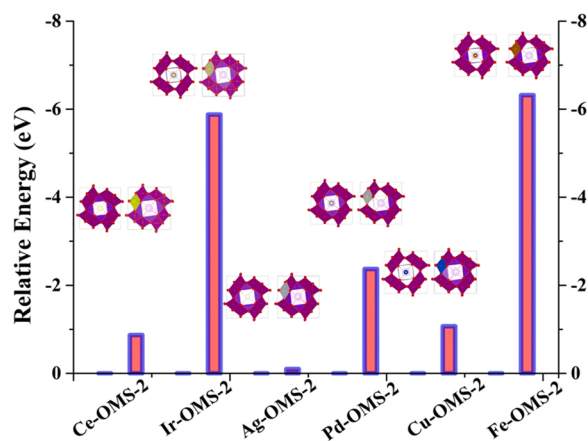


Fig. 6. Relative energy of substitution of K hexahedral sites or Mn octahedral sites in OMS-2 by different metal ions.

to  $\text{Ag}^+$  species [17,43]. The XPS binding energy of Pd  $3d_{5/2}$  for Pd-OMS-2 is 337.2 eV, as shown in Fig. 7(D), indicating that  $\text{Pd}^{4+}$  is the predominant chemical state [44]. As demonstrated in Fig. 7(E), a strong  $\text{Cu}^{2+}$  satellite peak can be observed, implying that Cu ions exist in the form of  $\text{Cu}^{2+}$  in Cu-OMS-2 [38,45]. After deconvolution of Fe  $2p_{3/2}$  as illustrated in Fig. 7(F) [18],  $\text{Fe}^{3+}$  was found to account for about 73 % of total iron. Thus  $\text{Fe}^{3+}$  is the main chemical state with a minor contribution from  $\text{Fe}^{2+}$  ions.

The chemical states of skeleton Mn ions were investigated via Mn-K XANES and XPS of Mn 3s, as illustrated in Fig. 8 and Fig. S12 respectively. All M-OMS-2 catalysts exhibited XANES spectra similar to those of the pristine OMS-2 and the  $\text{MnO}_2$  reference sample as shown in Fig. 8 (A) and (B), but their spectra are quite different from the reference spectra of Mn foil, MnO, and  $\text{Mn}_2\text{O}_3$ . This indicates that  $\text{Mn}^{4+}$  is dominant in all M-OMS-2 materials. The average oxidation state (AOS) of M-OMS-2 was estimated to range from 3.53 to 3.87 as listed in Table S5, confirming that  $\text{Mn}^{4+}$  is dominant. Ir, Ag, Pd, Fe addition lowered the AOS values of Mn ions, indicative of an increase in  $\text{Mn}^{3+}$  (i. e. oxygen vacancies) [17,20]. In order to investigate the oxygen species, the O1s XPS spectra were deconvoluted as shown in Fig. S13. The specific peak positions and relative contents of different oxygen species are also summarized in Table S5. Metal addition clearly decreased the relative content of surface oxygen ( $\text{O}_\text{p}$ , BE = 531.5 eV) [25,28] and



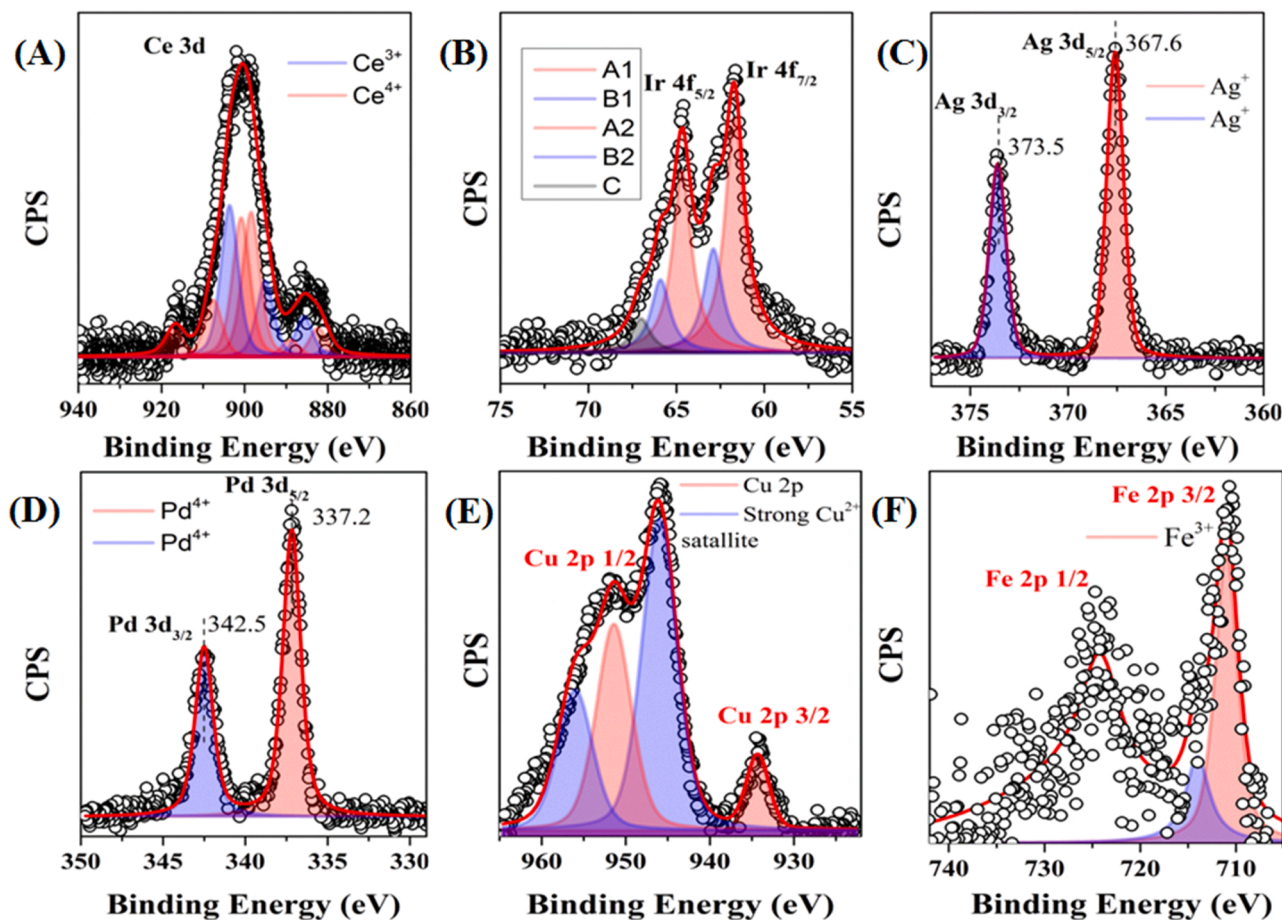


Fig. 7. The XPS binding energies of Ce 3d (A), Ir 4f (B), Ag 3d (C), Pd 3d (D), Cu 2p (E) and Fe 2p (F) for the corresponding M-OMS-2 samples.

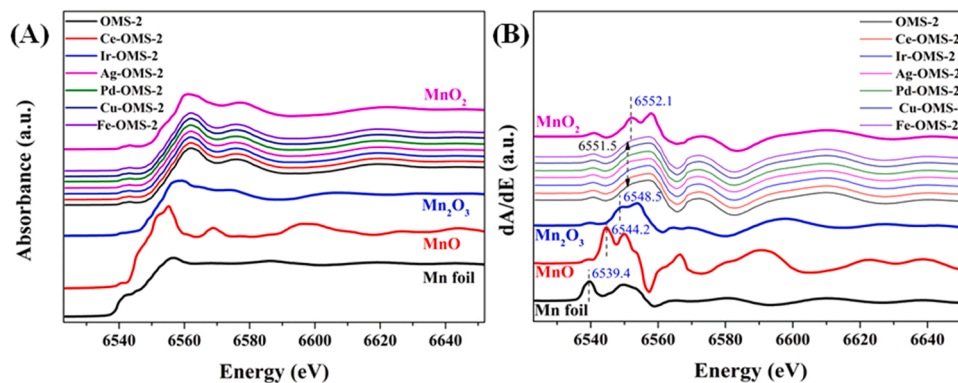


Fig. 8. Normalized Mn K-edge XANES spectra of different M-OMS-2 catalysts (A) and the corresponding first-order derivatives of XANES (B).

adsorbed water ( $O_{\gamma}$ , BE = 533.0 eV) [25,28] compared to pristine OMS-2. This indicates that the properties of surface oxygen species are inevitably modulated by metal doping.

The reducibility of M-OMS-2 catalysts was investigated by means of  $H_2$ -TPR as shown in Fig. 9(A). The noble metals Ir, Pd and Ag embedded into the OMS-2 caused the main reduction peaks to move significantly toward lower temperatures. For instance, the two equivalent reduction peaks of OMS-2, attributed to the reduction of  $MnO_2$  to  $Mn_2O_3$  and then to  $MnO$  [17,38,40], were at 305 and 325 °C respectively, while Pd addition caused the equivalent peaks to move to 90 and 100 °C respectively.

Hence, the reducibility of Pd-OMS-2, Ir-OMS-2 and Ag-OMS-2 was significantly enhanced. Other metals including Ce, Cu, Fe barely moved

the main reduction peak, but the profiles were altered due to the mixed valence of the incorporated metal ions. In order to learn the mobility of oxygen species in M-OMS-2, a CO-TPD experiment was also performed as illustrated in Fig. 9(B). The  $CO_2$  desorption branch revealed that Pd-OMS-2 and Ag-OMS-2 have relatively high oxygen mobility, since the desorption of  $CO_2$  occurs at lower temperatures. Pd, Ir and Ce doping remarkably activated the lattice oxygen of OMS-2 as seen by the enhancement of  $CO_2$  desorption compared to that of other M-OMS-2.

#### 3.4. Mechanism for the excellent tunable activity of M-OMS-2 in eliminating various VOC species

In order to examine the changes in the local structure of M-OMS-2



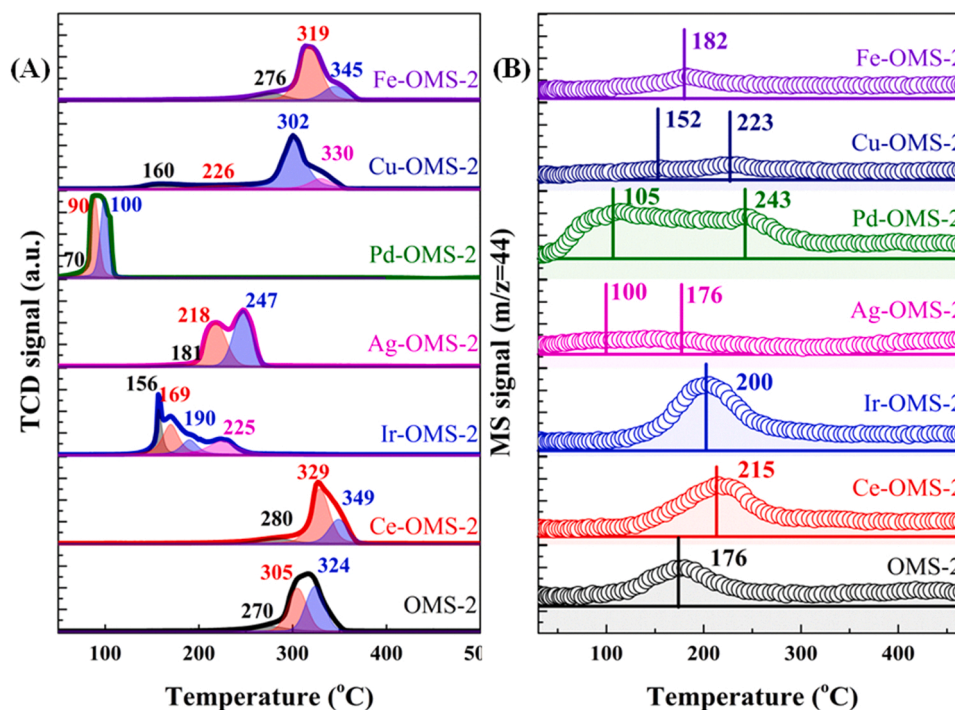


Fig. 9.  $\text{H}_2$ -TPR profiles (A) and CO-TPD profile  $\text{CO}_2$  branch (B) of M-OMS-2 catalysts.

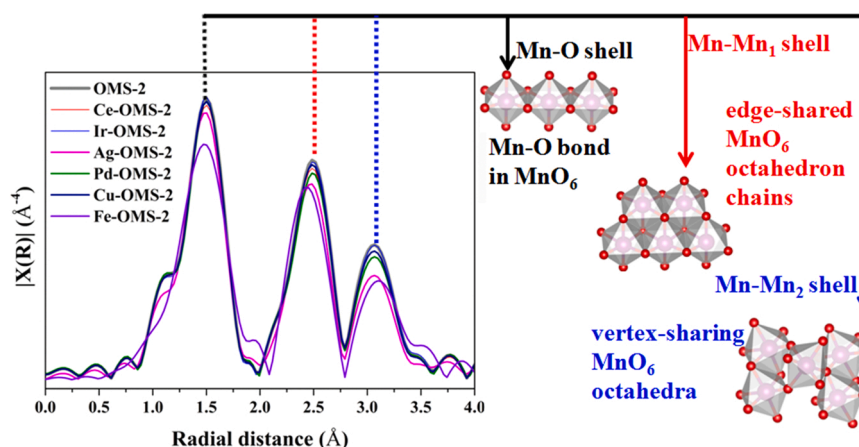


Fig. 10. EXAFS spectra of Mn K-edge in series of M-OMS-2 catalysts and local structure models of different coordination shells.

after addition of different metals, the X-ray absorption fine structure of the Mn-K edge was measured. Fig. 10 shows the radial distribution function of the Mn K-edge in the series of M-OMS-2 catalysts. Consistent with many other reports [17,18,39], the bond distance at 1.90 Å was assigned to Mn-O bonds in  $\text{MnO}_6$  octahedra as depicted in Fig. 10. A peak at ca. 2.90 Å could be assigned to the Mn-Mn<sub>1</sub> shell originating from edge-shared  $\text{MnO}_6$  octahedron chains. The peak at ca. 3.40 Å could be ascribed to the Mn-Mn<sub>2</sub> shell from vertex-sharing  $\text{MnO}_6$  octahedra. The coordination results and fitted data are presented in Table 3 and Fig. S14.

It is worthy of note that the X-ray absorption energy of the Fe-K edge is 7112 eV, which is very close to that of the Mn-K edge (6539 eV). Thus, the Mn-K edge extended X-ray absorption fine structure spectrum of Fe-OMS-2 was disturbed by the presence of Fe. Therefore, the local structure of Fe-OMS-2 is not likely to be well revealed by EXAFS. Compared to pristine OMS-2, the coordination numbers associated with different shells of Ce-OMS-2, Ir-OMS-2, and Cu-OMS-2 decreased to various degrees as shown in Fig. 10 and Table 3.  $\text{Pd}^{4+}$  and  $\text{Ag}^+$  incorporated in

OMS-2 changed the local structure to the greatest extent, due to their lower coordination numbers. However, the VOC removal efficiency is not directly associated with coordination defects, since Pd-OMS-2 and Ag-OMS-2 had high numbers of defects but did not exhibit excellent activity in the oxidation of acetone and dichloromethane.

It is widely accepted that the reducibility and mobility of oxygen species in catalysts generally determine the catalytic combustion activity [1,5].  $\text{Mn}^{3+}$ /oxygen vacancies in  $\text{MnO}_2$  are considered to play a key role in enhancing activity via activating oxygen. However, as illustrated in Fig. 1 and Table 1, Cu-OMS-2 and Ir-OMS-2 have the highest specific activity for eliminating acetone and dichloromethane respectively, but the activity of their oxygen species as well as their amounts of defects is not remarkable, as illustrated in Fig. 9 and Table 3. Hence, the active oxygen species on the surface of catalysts might be not the sole decisive factor affecting the oxidation efficiency. The molecular activation and reaction pathway of VOCs may also play critical roles in combustion that may often be ignored.

For this reason, thermal desorption-gas chromatography-mass

**Table 3**  
Curve-fitting results of Mn-K EXAFS for different M-OMS-2 samples.

Sample	Shell	CN	R (Å)	$\sigma^2$ ( $\times 10^{-3}$ Å <sup>2</sup> )	R Factor (%)
OMS-2	(Mn-O,	(5.44 ± 0.3,	(1.89 ± 0.1,	4.32	0.78
	Mn-Mn1,	3.30 ± 0.3,	2.89 ± 0.1,		
	Mn-Mn2)	3.28 ± 0.4)	3.45 ± 0.1)		
Ce-OMS-2	(Mn-O,	(5.32 ± 0.3,	(1.90 ± 0.1,	4.33	0.77
	Mn-Mn1,	3.18 ± 0.3,	2.89 ± 0.1,		
	Mn-Mn2)	3.12 ± 0.3)	3.44 ± 0.1)		
Ir-OMS-2	(Mn-O,	(5.36 ± 0.3,	(1.90 ± 0.1,	4.19	0.71
	Mn-Mn1,	3.21 ± 0.3,	2.89 ± 0.1,		
	Mn-Mn2)	3.18 ± 0.1)	3.45 ± 0.1)		
Ag-OMS-2	(Mn-O,	(5.38 ± 0.3,	(1.89 ± 0.1,	4.62	0.86
	Mn-Mn1,	3.06 ± 0.3,	2.88 ± 0.1,		
	Mn-Mn2)	2.73 ± 0.3)	3.44 ± 0.1)		
Pd-OMS-2	(Mn-O,	(5.28 ± 0.3,	(1.89 ± 0.1,	4.16	0.91
	Mn-Mn1,	3.03 ± 0.3,	2.89 ± 0.1,		
	Mn-Mn2)	2.89 ± 0.4)	3.44 ± 0.1)		
Cu-OMS-2	(Mn-O,	(5.36 ± 0.3,	(1.90 ± 0.1,	4.29	0.76
	Mn-Mn1,	3.22 ± 0.3,	2.89 ± 0.1,		
	Mn-Mn2)	3.10 ± 0.3)	3.44 ± 0.1)		
Fe-OMS-2	(Mn-O,	(4.96 ± 0.5,	(1.90 ± 0.1,	4.28	1.31
	Mn-Mn1,	3.05 ± 0.4,	2.89 ± 0.1,		
	Mn-Mn2)	2.90 ± 0.5)	3.44 ± 0.1)		

spectrometry tests were conducted at different reaction temperatures to learn the VOC reaction pathways, as shown in Fig. S15. Benzaldehyde is one of the most prominent intermediates in toluene oxidation. Acetic acid is the main intermediate for acetone combustion via C—C bond cleavage. 1, 2, dichloride, trichloromethane and trichloroacetyl chloride are observed in dichloromethane oxidation at low temperatures, as illustrated in Fig. S15(C), indicating that cleavage of the C—Cl bond in dichloromethane is the vital step for its complete oxidation. Our GC-MS results are consistent with many other reports [30,46,47] and the molecular oxidation pathways of the above three kinds of VOCs are summarized in Fig. S16.

In order to determine the surface mechanism and discern the role of selected M-OMS-2 catalysts in VOC activation, VOC-TPD and TPSR experiments were performed and illustrated in Figs. 11 and S17 respectively. TPSR with excess oxygen revealed that the CO<sub>2</sub> profiles are similar to the TPD results without gas-phase oxygen. This implies that the surface lattice oxygen of M-OMS-2 is highly active. The reaction

pathway for VOC oxidation over M-OMS-2 likely follows the Mars-Van-Krevelen mechanism.

Different kinds of intermediates were recorded in the TPD profiles to investigate the activation of specific VOC species. Compared to pristine OMS-2, Pd-OMS-2 demonstrated enhanced formation of C<sub>6</sub>H<sub>6</sub> and CO<sub>2</sub>, and desorption of C<sub>7</sub>H<sub>8</sub> was depressed, as shown in Fig. 11(A). This indicated that Pd addition clearly boosts the oxidation of toluene via enhancing the formation of intermediates. Moreover, the dissociation products of acetone generated via C—C bond cleavage are CH<sub>3</sub>CHO and HCHO etc. [30,46,48], which were detected during acetone-TPD as shown in Fig. 11(B). Cu-OMS-2 exhibited enhanced formation of HCHO species and the desired product CO<sub>2</sub>. Hence, Cu species clearly demonstrated good ability for the elimination of acetone via activating C—C bonds. Dichloromethane is relatively hard to remove, and C—Cl bond cleavage is the vital step [47,49]. The profiles of intermediates and final products originating from CH<sub>2</sub>Cl<sub>2</sub> oxidation are shown in Fig. 11(C). The intermediate HCOOH derived from C—Cl bond cleavage was clearly observed over Ir-OMS-2, which also exhibited the best activity in the abatement of CH<sub>2</sub>Cl<sub>2</sub> as verified in Fig. 1(C). Thus, Ir species could be confirmed as the best sites in M-OMS-2 to remove dichloromethane via dissociation of the C—Cl bond.

In brief, the combined results of XRD, Raman, HRTEM, mapping, ICP-OES and EXAFS revealed that Pd, Cu and Ir cations substitute for Mn on octahedral sites in the OMS-2 lattice, forming catalysts with highly dispersed dopants. Apart from the key role played by surface active oxygen species in VOC oxidation, the heteroatom sites introduced in M-OMS-2 influence the activation of VOC molecules to a great extent, which was found to play a critical role in VOC oxidation.

#### 4. Conclusions

In summary, different metals could be well-dispersed into the lattice of OMS-2 without changing the crystal structure, as testified by XRD, Raman, and TEM results. Elemental mapping images and ICP-OES combined with DFT calculations revealed that Ce, Ir, Pd, Cu and Fe were incorporated into the OMS-2 framework by substituting for Mn ions, and Ag could be stabilized in the tunnel of OMS-2 via replacement of K ions. EXAFS results suggest that the local tunnel structures of OMS-2 were almost intact after incorporation of the different metals. The CO and VOC-TPD results demonstrated that Pd-OMS-2 and Ag-OMS-2 exhibited excellent activity in the catalytic oxidation of toluene owing

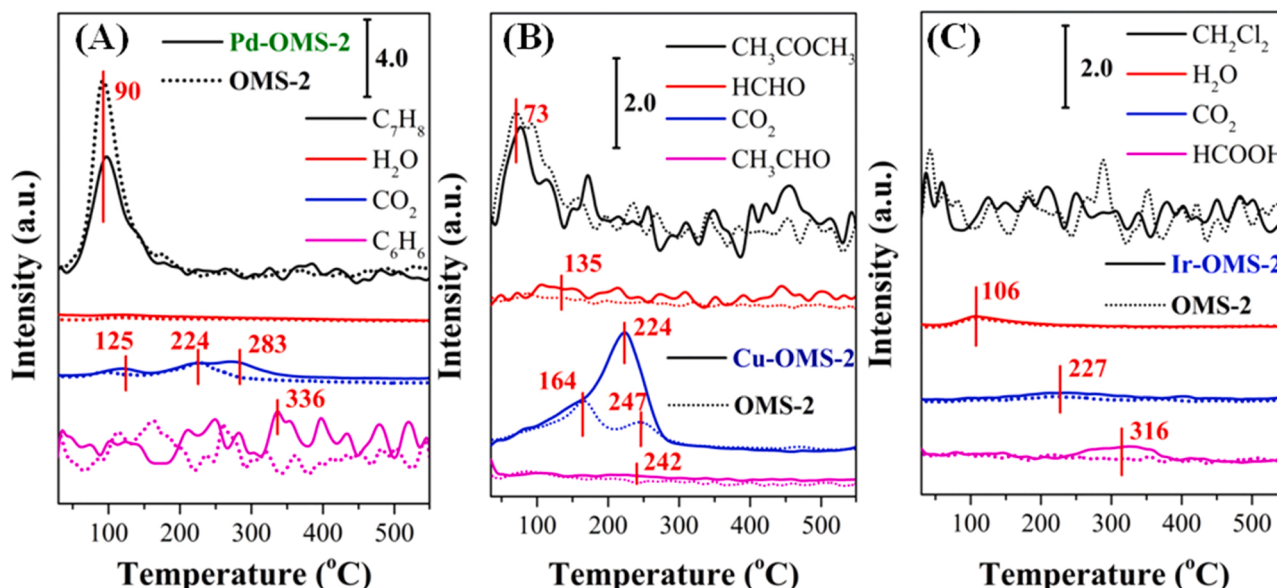


Fig. 11. VOC-TPD profiles of OMS-2 and optimized M-OMS-2 catalysts, (A) toluene, (B) acetone, and (C) dichloromethane.

to the improved reducibility and mobility of oxygen. Cu-OMS-2 showed the highest activity in the removal of acetone by means of facile C—C bond breaking. Ir-OMS-2 demonstrated specific activity in the elimination of dichloromethane via facile cleavage of the C—Cl bond. This work provides intrinsic catalytic mechanisms and describes the behavior of metal ion dopants with high catalytic oxidation activity toward specific VOC species, and may assist in the design and preparation of flexible catalysts for control of miscellaneous VOCs.

### CRedit authorship contribution statement

**Hua Deng:** Conceptualization, Writing – original draft, Resources. **Tingting Pan:** Investigation, Data curation. **Yuqing Lu:** Investigation, Data curation. **Lian Wang:** Writing – review & editing. **Changbin Zhang:** Writing – review & editing. **Hong He:** Writing – review & editing, Supervision, Funding acquisition, Project administration.

### Declaration of Competing Interest

The authors declare that they have no known competing financial interests or personal relationships that could have appeared to influence the work reported in this paper.

### Data Availability

Data will be made available on request.

### Acknowledgements

The work was supported by the Youth Innovation Promotion Association, Chinese Academy of Sciences (2019306), the National Natural Science Foundation of China (21936005), the Cultivating Project of Strategic Priority Research Program of Chinese Academy of Sciences (Grant no. XDPB1902), Central Funds Guiding the Local Science and Technology Development (2020L3023) and the Science and Technology Planning Project of Xiamen City (No. 3502220191021).

### Appendix A. Supporting information

Supplementary data associated with this article can be found in the online version at [doi:10.1016/j.apcatb.2022.121955](https://doi.org/10.1016/j.apcatb.2022.121955).

### References

- [1] Y.L. Guo, M.C. Wen, G.Y. Li, T.C. An, Recent advances in VOC elimination by catalytic oxidation technology onto various nanoparticles catalysts: a critical review, *Appl. Catal. B-Environ.* 281 (2021), 119447.
- [2] Y. Ma, L. Wang, J.Z. Ma, H.H. Wang, C.B. Zhang, H. Deng, H. He, Investigation into the enhanced catalytic oxidation of o-xylene over MOF-derived Co3O4 with different shapes: the role of surface twofold-coordinate lattice oxygen (O-2f), *ACS Catal.* 11 (2021) 6614–6625.
- [3] B. Li, S.S.H. Ho, X. Li, L. Guo, A. Chen, L. Hu, Y. Yang, D. Chen, A. Lin, X. Fang, A comprehensive review on anthropogenic volatile organic compounds (VOCs) emission estimates in China: comparison and outlook, *Environ. Int.* 156 (2021).
- [4] M. Li, Q. Zhang, B. Zheng, D. Tong, Y. Lei, F. Liu, C.P. Hong, S.C. Kang, L. Yan, Y. X. Zhang, Y. Bo, H. Su, Y.F. Cheng, K.B. He, Persistent growth of anthropogenic non-methane volatile organic compound (NMVOC) emissions in China during 1990–2017: drivers, speciation and ozone formation potential, *Atmos. Chem. Phys.* 19 (2019) 8897–8913.
- [5] C. He, J. Cheng, X. Zhang, M. Douthwaite, S. Pattison, Z. Hao, Recent advances in the catalytic oxidation of volatile organic compounds: a review based on pollutant sorts and sources, *Chem. Rev.* 119 (2019) 4471–4568.
- [6] T. Zhang, X.Y. Lang, A.Q. Dong, X. Wan, G. Shan, L. Wang, L.X. Wang, W.C. Wang, Difference of oxidation mechanism between light C3–C4 alkane and alkene over mullite YMn2O5 oxides' catalyst, *ACS Catal.* 10 (2020) 7269–7282.
- [7] Y. Guo, M. Wen, S. Song, Q. Liu, G. Li, T. An, Enhanced catalytic elimination of typical VOCs over ZnCoOx catalyst derived from in situ pyrolysis of ZnCo bimetallic zeolitic imidazolate frameworks, *Appl. Catal. B-Environ.* 308 (2022), 121212.
- [8] W. Wei, S.X. Wang, J.M. Hao, S.Y. Cheng, Trends of chemical speciation profiles of anthropogenic volatile organic compounds emissions in China, 2005–2020, *Front. Environ. Sci. Eng.* 8 (2014) 27–41.
- [9] X.T. Mu, H.L. Ding, W.G. Pan, Q. Zhou, W. Du, K.N. Qiu, J.C. Ma, K. Zhang, Research progress in catalytic oxidation of volatile organic compound acetone, *J. Environ. Chem. Eng.* 9 (2021).
- [10] S.Y. Lei, S.J. Guo, X.L. Sun, H. Yu, F. Xu, N. Wan, Z.A. Wang, Capture and dissociation of dichloromethane on Fe, Ni, Pd and Pt decorated phosphorene, *Appl. Surf. Sci.* 495 (2019), 143533.
- [11] P. Wu, X. Jin, Y. Qiu, D. Ye, Recent progress of thermocatalytic and photo/thermocatalytic oxidation for VOCs purification over manganese-based oxide catalysts, *Environ. Sci. Technol.* 55 (2021) 4268–4286.
- [12] Y. Zheng, Q. Liu, C. Shan, Y. Su, K. Fu, S. Lu, R. Han, C. Song, N. Ji, D. Ma, Defective ultrafine MnOx nanoparticles confined within a carbon matrix for low-temperature oxidation of volatile organic compounds, *Environ. Sci. Technol.* 55 (2021) 5403–5411.
- [13] L.F. Liotta, Catalytic oxidation of volatile organic compounds on supported noble metals, *Appl. Catal. B-Environ.* 100 (2010) 403–412.
- [14] X.Q. Wu, R. Han, Q.L. Liu, Y. Su, S.C. Lu, L.Z. Yang, C.F. Song, N. Ji, D.G. Ma, X. B. Lu, A review of confined-structure catalysts in the catalytic oxidation of VOCs: synthesis, characterization, and applications, *Catal. Sci. Technol.* 11 (2021) 5374–5387.
- [15] M. Sun, W.P. Li, B.T. Zhang, G. Cheng, B. Lan, F. Ye, Y.Y. Zheng, X.L. Cheng, L. Yu, Enhanced catalytic performance by oxygen vacancy and active interface originated from facile reduction of OMS-2, *Chem. Eng. J.* 331 (2018) 626–635.
- [16] C.K. King'andu, N. Opembe, C.H. Chen, K. Ngala, H. Huang, A. Iyer, H.F. Garces, S. L. Suib, Manganese oxide octahedral molecular sieves (OMS-2) multiple framework substitutions: a new route to OMS-2 particle size and morphology control, *Adv. Funct. Mater.* 21 (2011) 312–323.
- [17] H. Deng, S. Kang, J. Ma, C. Zhang, H. He, Silver incorporated into cryptomelane-type manganese oxide boosts the catalytic oxidation of benzene, *Appl. Catal. B-Environ.* 239 (2018) 214–222.
- [18] J.Z. Ma, C.X. Wang, H. He, Transition metal doped cryptomelane-type manganese oxide catalysts for ozone decomposition, *Appl. Catal. B-Environ.* 201 (2017) 503–510.
- [19] G. He, M. Gao, Y. Peng, Y. Yu, W. Shan, H. He, Superior oxidative dehydrogenation performance toward NH3 determines the excellent low-temperature NH3-SCR activity of Mn-based catalysts, *Environ. Sci. Technol.* 55 (2021) 6995–7003.
- [20] J.T. Hou, L.L. Liu, Y.Z. Li, M.Y. Mao, H.Q. Lv, X.J. Zhao, Tuning the K<sup>+</sup> concentration in the tunnel of OMS-2 nanorods leads to a significant enhancement of the catalytic activity for benzene oxidation, *Environ. Sci. Technol.* 47 (2013) 13730–13736.
- [21] X. Yang, X. Ma, D. Han, M. Xiao, L. Ma, H. Sun, X. Yu, M. Ge, Efficient removal of toluene over palladium supported on hierarchical alumina microspheres catalyst, *Catal. Today* 375 (2021) 352–359.
- [22] F. Bi, X. Zhang, J. Chen, Y. Yang, Y. Wang, Excellent catalytic activity and water resistance of UiO-66-supported highly dispersed Pd nanoparticles for toluene catalytic oxidation, *Appl. Catal. B-Environ.* 269 (2020), 118767.
- [23] X. Wan, L. Wang, S. Gao, X. Lang, L. Wang, T. Zhang, A. Dong, W. Wang, Low-temperature removal of aromatics pollutants via surface labile oxygen over Mn-based mullite catalyst SmMn2O5, *Chem. Eng. J.* 410 (2021), 128305.
- [24] P. Wang, J. Wang, X. An, J. Shi, W. Shanguan, X. Hao, G. Xu, B. Tang, A. Abudula, G. Guan, Generation of abundant defects in Mn-Co mixed oxides by a facile agar gel method for highly efficient catalysis of total toluene oxidation, *Appl. Catal. B-Environ.* 282 (2021), 119560.
- [25] W. Yang, Z. Su, Z. Xu, W. Yang, Y. Peng, J. Li, Comparative study of  $\alpha$ -,  $\beta$ -,  $\gamma$ - and  $\delta$ -MnO2 on toluene oxidation: oxygen vacancies and reaction intermediates, *Appl. Catal. B-Environ.* 260 (2020), 118150.
- [26] J. Niu, H. Liu, H. Qian, J. Liu, M. Ma, E. Duan, L. Yu, Preparation of metal-doped Cu-Mn/HTS-1 catalysts and their mechanisms in efficient degradation of toluene, *J. Environ. Sci.* 88 (2020) 260–272.
- [27] Y. Zheng, Q. Zhao, C. Shan, S. Lu, Y. Su, R. Han, C. Song, N. Ji, D. Ma, Q. Liu, Enhanced acetone oxidation over the Cu2O/Co3O4 catalyst derived from metal-organic frameworks, *ACS Appl. Mater. Interfaces* 12 (2020) 28139–28147.
- [28] A.Q. Dong, S. Gao, X. Wan, L.X. Wang, T. Zhang, L. Wang, X.Y. Lang, W.C. Wang, Labile oxygen promotion of the catalytic oxidation of acetone over a robust ternary Mn-based mullite GdMn2O5, *Appl. Catal. B-Environ.* 271 (2020), 118932.
- [29] J.H. Chen, X.N. Yu, X.C. Zhu, C.H. Zheng, X. Gao, K.F. Cen, Electrospinning synthesis of vanadium-TiO2-carbon composite nanofibrous membranes as effective catalysts for the complete oxidation of low-concentration acetone, *Appl. Catal. A-Gen.* 507 (2015) 99–108.
- [30] Y.G. Sun, X. Zhang, N. Li, X. Xing, H.L. Yang, F.L. Zhang, J. Cheng, Z.S. Zhang, Z. P. Hao, Surface properties enhanced MnAlOx oxide catalysts derived from MnAl layered double hydroxides for acetone catalytic oxidation at low temperature, *Appl. Catal. B-Environ.* 251 (2019) 295–304.
- [31] Z.W. Wang, S. Li, S.H. Xie, Y.X. Liu, H.X. Dai, G.S. Guo, J.G. Deng, Supported ultralow loading Pt catalysts with high H2O-, CO2-, and SO2-resistance for acetone removal, *Appl. Catal. A-Gen.* 579 (2019) 106–115.
- [32] T. Kondratowicz, M. Drozdek, M. Michalik, W. Gac, M. Gajewska, P. Kustrowski, Catalytic activity of Pt species variously dispersed on hollow ZrO2 spheres in combustion of volatile organic compounds, *Appl. Surf. Sci.* 513 (2020), 145788.
- [33] L. Zhang, S.S. Huang, W. Deng, D.Y. Yang, Q.X. Tang, S.M. Zhu, L.M. Guo, Dichloromethane catalytic combustion over Co3O4 catalysts supported on MFI type zeolites, *Microporous Mesoporous Mater.* 312 (2021), 110599.
- [34] H.Q. Xia, H. Zhang, J.Y. Wu, G. Chen, W. Sun, S.J. Shao, Q.G. Dai, X.Y. Wang, Oxidative decomposition of dichloromethane over sulfated iron titanate catalysts: catalytic performance and reaction mechanism, *Appl. Catal. A-Gen.* 616 (2021), 118094.



- [35] Y. Su, K.X. Fu, Y.F. Zheng, N. Ji, C.F. Song, D.G. Ma, X.B. Lu, R. Han, Q.L. Liu, Catalytic oxidation of dichloromethane over Pt-Co/HZSM-5 catalyst: synergistic effect of single-atom Pt,  $\text{Co}_3\text{O}_4$ , and HZSM-5, *Appl. Catal. B-Environ.* 288 (2021), 119980.
- [36] Q.J. Ying, Y. Liu, N.Y. Wang, Y.Y. Zhang, Z.B. Wu, The superior performance of dichloromethane oxidation over Ru doped sulfated  $\text{TiO}_2$  catalysts: synergistic effects of Ru dispersion and acidity, *Appl. Surf. Sci.* 515 (2020), 145971.
- [37] X.Q. Fei, W.L. Ouyang, Z.Y. Gu, S. Cao, H.Q. Wang, X.L. Weng, Z.B. Wu, Effect of Cr doping in promoting the catalytic oxidation of dichloromethane ( $\text{CH}_2\text{Cl}_2$ ) over Cr-Co@Z catalysts, *J. Hazard. Mater.* 413 (2021), 125327.
- [38] Y. Yang, J. Huang, S.Z. Zhang, S.W. Wang, S.B. Deng, B. Wang, G. Yu, Catalytic removal of gaseous HCBz on Cu doped OMS: Effect of Cu location on catalytic performance, *Appl. Catal. B-Environ.* 150 (2014) 167–178.
- [39] C. Wang, J. Ma, F. Liu, H. He, R. Zhang, The effects of  $\text{Mn}^{2+}$  precursors on the structure and ozone decomposition activity of cryptomelane-type manganese oxide (OMS-2) catalysts, *J. Phys. Chem. C* 119 (2015) 23119–23126.
- [40] A.M. El-Sawy, C.K. King'ondeu, C.H. Kuo, D.A. Kriz, C.J. Guild, Y.T. Meng, S. J. Frueh, S. Dharmarathna, S.N. Ehrlich, S.L. Suib, X-ray absorption spectroscopic study of a highly thermally stable manganese oxide octahedral molecular sieve (OMS-2) with high oxygen reduction reaction activity, *Chem. Mater.* 26 (2014) 5752–5760.
- [41] A. Iyer, J. Del-Pilar, C.K. King'ondeu, E. Kissel, H.F. Garces, H. Huang, A.M. El-Sawy, P.K. Dutta, S.L. Suib, Water oxidation catalysis using amorphous manganese oxides, octahedral molecular sieves (OMS-2), and octahedral layered (OL-1) manganese oxide structures, *J. Phys. Chem. C* 116 (2012) 6474–6483.
- [42] L. Atanasoska, R. Atanasoski, S. Trasatti, XPS and AES study of mixed layers of  $\text{RuO}_2$  and  $\text{IrO}_2$ , *Vacuum* 40 (1990) 91–94.
- [43] J.L. Chen, J. Li, H.J. Li, X.M. Huang, W.J. Shen, Facile synthesis of Ag-OMS-2 nanorods and their catalytic applications in CO oxidation, *Microporous Mesoporous Mater.* 116 (2008) 586–592.
- [44] O. Lupan, V. Postica, M. Hoppe, N. Wolff, O. Polonskyi, T. Pauporte, B. Viana, O. Majerus, L. Kienle, F. Faupel, R. Adelung, PdO/PdO<sub>2</sub> functionalized ZnO: Pd films for lower operating temperature  $\text{H}_2$  gas sensing, *Nanoscale* 10 (2018) 14107–14127.
- [45] Y. Jiang, Q. Gao, Preparation of  $\text{Cu}^{2+/+}$ -VSB-5 and their catalytic properties on hydroxylation of phenol, *Mater. Lett.* 61 (2007) 2212–2216.
- [46] Z.W. Wang, P.J. Ma, K. Zheng, C. Wang, Y.X. Liu, H.X. Dai, C.C. Wang, H.C. Hsi, J. G. Deng, Size effect, mutual inhibition and oxidation mechanism of the catalytic removal of a toluene and acetone mixture over  $\text{TiO}_2$  nanosheet-supported Pt nanocatalysts, *Appl. Catal. B-Environ.* 274 (2020), 118963.
- [47] F.W. Lin, Z.M. Zhang, N. Li, B.B. Yan, C. He, Z.P. Hao, G.Y. Chen, How to achieve complete elimination of Cl-VOCs: a critical review on byproducts formation and inhibition strategies during catalytic oxidation, *Chem. Eng. J.* 404 (2021), 126534.
- [48] C.L. Bianchi, S. Gatto, C. Pirola, A. Naldoni, A. Di Michele, G. Cerrato, V. Crocella, V. Capucci, Photocatalytic degradation of acetone, acetaldehyde and toluene in gas-phase: comparison between nano and micro-sized  $\text{TiO}_2$ , *Appl. Catal. B-Environ.* 146 (2014) 123–130.
- [49] X.L. Weng, Q.J. Meng, J.J. Liu, W.Y. Jiang, S. Pattison, Z.B. Wu, Catalytic oxidation of chlorinated organics over lanthanide perovskites: effects of phosphoric acid etching and water vapor on chlorine desorption behavior, *Environ. Sci. Technol.* 53 (2019) 884–893.